Journal of
Applied Remote Sensing

RemoteSensing.SPIEDigitalLibrary.org

Observation of sand waves in the Taiwan Banks using HJ-1A/1B sun glitter imagery

Hua-guo Zhang
Xiu-lin Lou
Ai-qin Shi
Xie-kai He
Wei-bing Guan
Dong-ling Li

SPIE.

Observation of sand waves in the Taiwan Banks using HJ-1A/1B sun glitter imagery

Hua-guo Zhang,[a] Xiu-lin Lou,[a,*] Ai-qin Shi,[a] Xie-kai He,[b] Wei-bing Guan,[a] and Dong-ling Li[a]

[a]State Key Laboratory of Satellite Ocean Environment Dynamics, Second Institute of Oceanography, State Oceanic Administration, Hangzhou 310012, China

[b]Zhejiang University, Department of Earth Science, Hangzhou 310027, China

Abstract. This study focuses on the large sand waves in the Taiwan Banks. Our goals are to observe the sand waves as completely as possible, to obtain their direction, wavelength, density, and ridge length, to analyze their spatial distributions, and to understand the effects of the current field and water depth on the sand waves. This study demonstrates the possibility of using HJ-1A/1B sun glitter imagery with a large swath width and rapid coverage in studying sand waves. Six cloud-free HJ-1A/1B optical images with sun glitter signals received during 2009 to 2011 were processed. The sand waves were mapped based on their features in the images; their direction, wavelength, density, and ridge length were measured and analyzed. We identified 4604 sand waves distributed in an area of 16,400 km^2. The distributions of sand waves and their characteristics were analyzed, and the differences of sand waves between the northwestern subregion and the southeastern subregion are reported. Further analysis and discussion of the relationships between spatial distribution of the sand waves and both the tidal current field from a numerical simulation and water depth led to some interesting conclusions. The current field determines the orientation of the sand wave, while the hydrodynamic conditions and water depth influence the shape, size, and density of sand waves to a certain degree. [DOI: 10.1117/1.JRS.8.083570]

Keywords: sand wave; the Taiwan Banks; sun glitter; remote sensing; HJ-1A/1B.

Paper 13522 received Dec. 11, 2013; revised manuscript received Jul. 2, 2014; accepted for publication Jul. 16, 2014; published online Aug. 12, 2014.

1 Introduction

Marine sand waves are a bottom morphology widely distributed in shallow marine environments. Their formation, migration, and spatial distribution have important influences on seabed stability, navigation safety, and pipeline engineering. Therefore, sand-wave mapping is of great significance in the fields of geology and oceanography. A multibeam bathymetry (MB) system is currently the most effective way of determining bathymetry and is becoming the standard instrument for hydrographic survey.[1] The MB data have been widely used in various marine research projects.[2–5] However, the sonar (sound navigation and ranging) method is expensive in terms of manpower and material resources for conducting a complete investigation. Nowadays, remote sensing has become an important and useful tool for observing and monitoring marine environments. In ocean color remote sensing, sun glitter is inevitably caused by specular reflection of sunlight from the sea surface directly into the sensor under certain imaging geometry conditions.[6] As a strong signal, sun glitter often interferes with the normal ocean color radiation signal, and therefore, sun glitter is considered as an intensive and negative factor for extracting accurate oceanic parameters using ocean color remote sensing images.[7] Avoidance of the influence of sun glitter has, therefore, become an important consideration for the design and application of ocean

*Address all correspondence to: Xiu-lin Lou, lxl@sio.org.cn

color remote sensing devices.[8] However, being a strong signal, sun glitter is also valuable in observing some oceanic features, such as internal waves, surface slick, and submarine bottom topography.[9–11] At considerably shallow water depths, submarine bottom hypsography can cause variations in the current field, which then influences surface flow field and, as a result, the sea surface roughness changes. With suitable imaging geometry, the change in sea surface roughness caused by submarine bottom topography, such as sand waves, is visible in sun glitter images that are obtained by satellite optical sensors.[7]

The largest marine sand waves in the world are found in the Taiwan Banks (TB), which is a shoal in the southern entrance of the Taiwan Strait between the South and East China Seas. In the past decades, considerable effort has been spent on surveying and studying the sand waves in the TB in order to understand the character of sand waves and its transfer.[12–15] The TB extend from the west near Dongshan Island on the Fujian coast to the east of the Penghu Islands, with its center at 23°00'N and 118°30'E (Fig. 1). The water depth in the TB is relatively shallow, from 10 to 35 m, with an average depth of 20 m. Due to coastal sediment and nonferrous materials, the highest water optical transparency in the TB is only ~30 m; especially in the nearshore zone, the water optical transparency ranges from 2 to 10 m.[16] Therefore, it is difficult for the visible radiance from the sun to reach the seafloor, and accordingly, it is more difficult to acquire the seafloor information using normal optical remote sensing images. However, the sun glitter images could record the changes in sea surface roughness caused by sand waves at a suitable imaging geometry because the depth of marine sand waves in the TB is very shallow. Further, comparing satellite imagery with MB data is a much more efficient, economic, and flexible way to survey sand waves because of its large swath width and rapid coverage. Satellite observations of sand waves in the TB have been previously conducted. For example, Li et al. first discussed the migration of sand waves in the TB using multitemporal space-borne synthetic aperture radar (SAR) imagery containing sand-wave information, by recording sea surface roughness.[17] Several other efforts were made to establish submarine bottom topography inversion models based on SAR remote sensing, considering only a few profiles or limited areas of the sand waves in the TB.[18–21] Shao took advantage of the sun glitter signals that appeared in satellite optical imagery to reconstruct some sand waves in the TB and to analyze their migrations.[7] Lian used a Thematic Mapper image from Landsat-5 satellite to extract the sand waves and to analyze their direction and wavelength based only on a few profiles.[22] Although considerable progress has been made on studying the sand waves in the TB, some aspects of these sand waves are yet to be completely deciphered. First of all, the complete coverage of the sand waves in the TB is still unresolved.

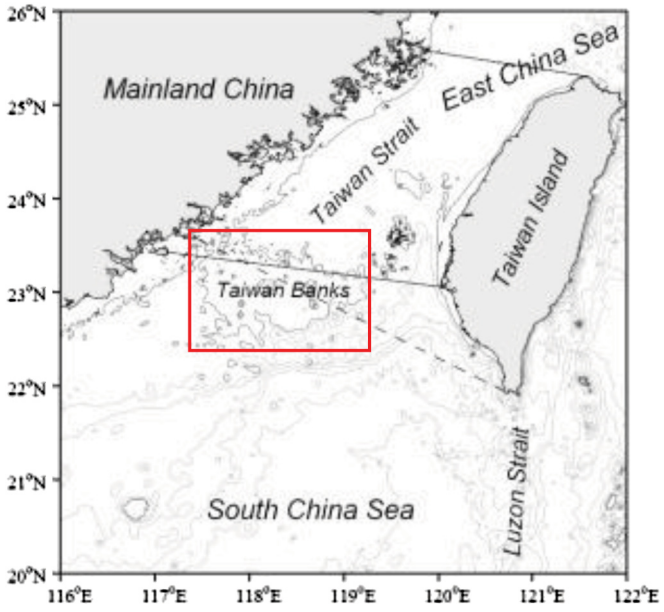

Fig. 1 Map of the study area, the Taiwan Banks (TB), which lies in the southern entrance of the Taiwan Strait.

Moreover, in addition to their direction and wavelength, their density (defined as the number of sand waves in a unit area) and ridge length are two important parameters of sand waves that are valuable for understanding the formation and shape of sand waves. Correa et al. studied the morphology and development of coral mounds based on quantitative analyses of a high-resolution geophysical dataset collected with an autonomous underwater vehicle.[23] However, the existing MB data in the TB are too limited for complete regional distribution, density, and ridge length of the sand waves. Density and the ridge length of sand waves in the TB have not been reported or addressed in the literature so far. Fortunately, remote sensing images with sun glitter provide us with a good opportunity for surveying the sand waves in the TB.

The major motivations for this study are to observe the sand waves in the TB as completely as possible, to obtain their direction, wavelength, density, and ridge length, to analyze their spatial distribution, and to understand the roles of the current field and water depth in shaping the sand waves. To take advantage of satellite remote sensing technology, multitemporal optical images with a large swath width obtained from the small satellite constellation for environment and disaster monitoring and forecasting (HJ-1A and HJ-1B, or HJ-1A/1B) were used to map and measure the sand waves in the TB. The study area of the TB and its geographic information are shown in Fig. 1.

2 Data and Methods

2.1 *HJ-1A/1B Charge-Coupled Device Data*

Multitemporal optical images from the HJ-1A/1B charge-coupled device (CCD) cameras are used in this study. The satellite constellation of HJ-1A/1B was launched on September 6, 2008, which was designed for environmental and disaster monitoring and forecasting. It is an ideal observation platform for daily monitoring of the environment and of the phenomena occurring over land and coastal oceans. The CCD cameras on-board HJ-1A/1B can acquire optical data in four channels covering the visible spectra from 430 to 900 nm, with a spatial resolution of 30 m and a swath width of 360 km. HJ-1A/1B CCD image data have been widely used in monitoring the environment and natural disasters, in terms of extracting disaster background information and assessing disaster damage.[24]

For this study, a total of 250 HJ-1A/1B images acquired from April 2009 to April 2012 were collected and investigated. Among them, 41 images containing sun glitter signals from submarine bottom topography in the TB were identified. Six cloud-free HJ-1A/1B CCD images were finally selected and processed to map and measure the sand waves in the TB. These six images are listed in Table 1. Figure 2 shows one of the six images covering the study area in true color imaged by HJ-1B CCD on May 15, 2009.

2.2 *Sun Glitter Imaging Mechanism of Submarine Bottom Topography*

According to previous research,[6] the signals of sun glitter radiation in ocean surface images are mainly dominated by the wind speed in suitable imaging geometry when there are no effects

Table 1 HJ-1A/1B CCD images used in this study.

No.	Satellite and sensor	Imaging date
1	HJ-1A CCD	13 May 2009
2	HJ-1B CCD	15 May 2009
3	HJ-1B CCD	24 July 2009
4	HJ-1B CCD	17 July 2010
5	HJ-1B CCD	17 August 2011
6	HJ-1B CCD	21 August 2011

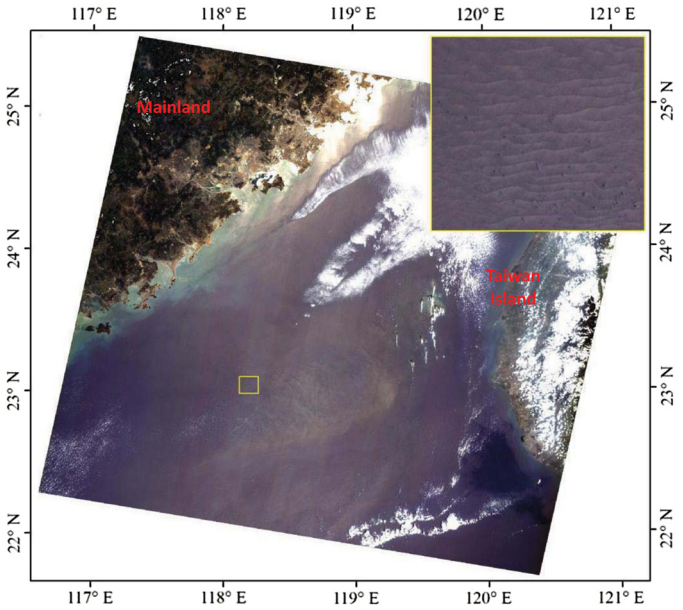

Fig. 2 The true color image covering the study area acquired by HJ-1B CCD on May 15, 2009. The subimage at the upper-right corner is the enlarged region in the yellow box, showing lots of bright and dark stripes induced by submarine sand waves.

from submarine bottom topography. However, when the sand waves are present and the water depth is considerably shallow, the sand wave hypsography will cause the current to change, influencing the sea surface flow field and sea surface roughness, and, in turn, affecting sun glitter signal intensity. The sun glitter radiation from the submarine sand waves will add to the background, and the sun glitter radiation of the region with submarine sand waves will appear conspicuously different from the adjacent region without sand waves. The response of sun glitter radiation to submarine bottom topography can be decomposed into the following four physical processes:[7] (1) forced modulation of the sea surface current due to submarine bottom topography; (2) modulation of the sea surface wave spectrum due to the changes in surface currents, through wave–current interaction, (3) impact of the sea surface roughness due to the changes in sea surface wave spectrum, and (4) modulation of the sun glitter radiation caused by the sea surface roughness.

2.3 *Determination of Sand Waves*

According to the imaging model of Alpers and Hennings,[25] referred to as the AH model, when the tidal flow direction is almost normal to the ridge, the sea surface roughness of the sand wave's upstream face (smooth face) is relatively smaller than that of the sand wave's downstream face (rough face). This implies that one side of the ridge has a smooth face and the other has a rough face. At a suitable imaging geometry, the smooth and the rough faces appear as bright and dark stripes in sun glitter images, respectively. In Fig. 3(a), which illustrates a case of a sun glitter image of HJ-1B containing sand-wave information, the sand waves appear as bright and dark stripes. Figure 3(b) shows pixel values along the red profile covering some sand waves as shown in Fig. 3(a). This also displays the change in pixel values while covering the sand-wave ridge. Figure 3(c) demonstrates corresponding water depths from MB along the same profile as in Fig. 3(a), which was obtained by R2Sonic 2024 broadband multibeam echo sounder device from May 25 to June 28 in 2012. Figures 3(b) and 3(c) show that the water depths and the pixel values vary asynchronously along the profile. In this case, it is evident that the location of a sand-wave ridge is between two adjacent bright and dark stripes, as shown in Fig. 3(b). Based on the sun glitter imaging mechanism of submarine sand waves, the sand waves and their ridges can be readily identified and drawn with the help of an image processing software, such as the ArcGIS platform. Figure 3(d) shows all the sand-wave ridges identified from the HJ-1B

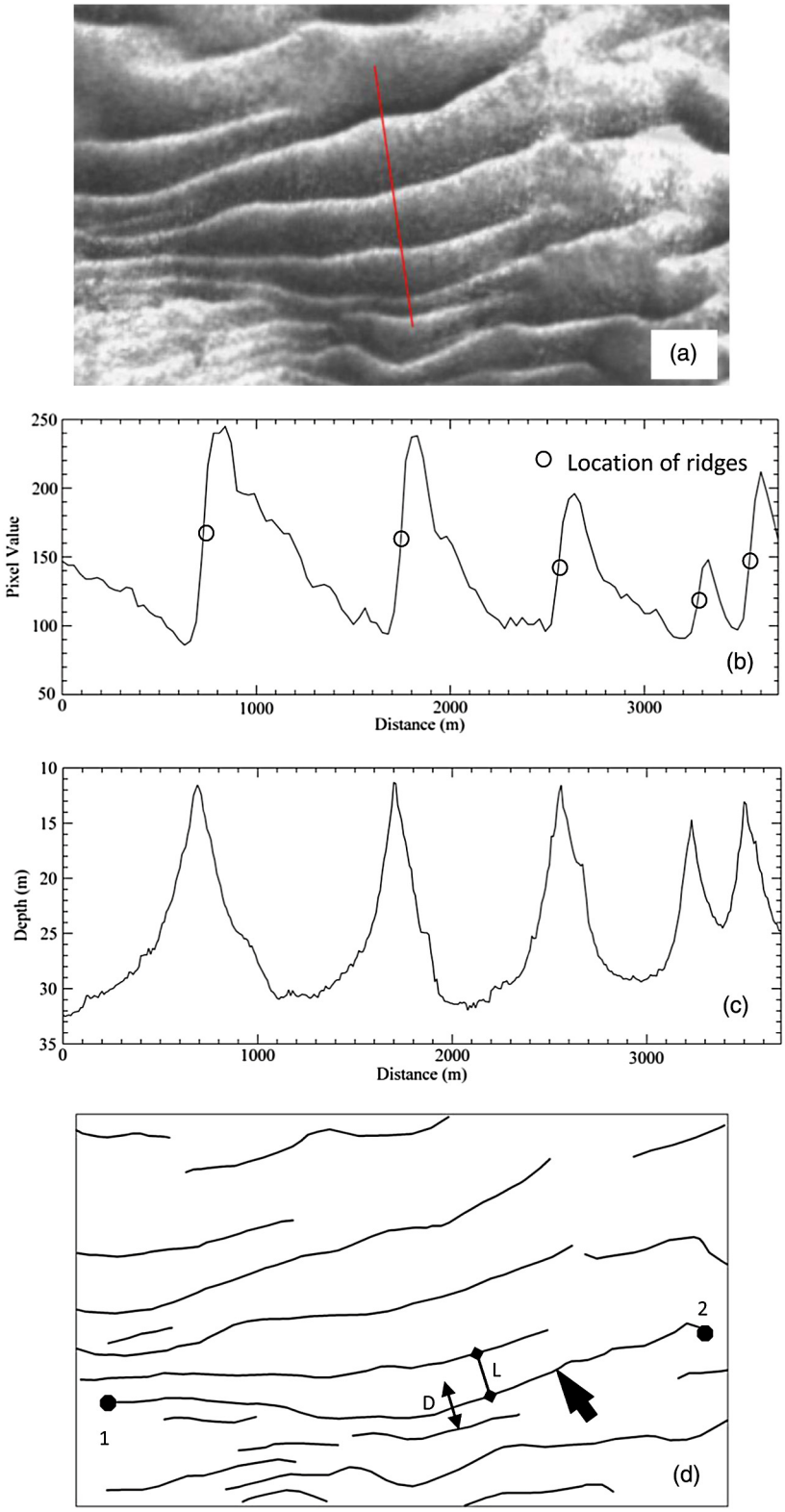

Fig. 3 Schematic determination of sand waves. (a) Sand-wave features in sun glitter image of HJ-1B and a red profile. (b) Pixel values along the profile in (a). (c) Water depths along the profile in (a). (d) Sand-wave ridges identified from (a). In the subimage (d), the length of L is the wavelength, the curve length from point "1" to "2" labeled by black arrow, and the direction of arrow labeled as D is the direction of the ridge curve labeled by black arrow.

image shown in Fig. 3(a). Limited by the spatial resolution of HJ-1A/B CCD imagery (30 m), our results indicate that a sand wave can be determined when its ridge length and wavelength are >200 and 100 m, respectively.

Following the determination of sand waves and their ridges, the directions, wavelengths, and ridge lengths of the sand waves can be measured and calculated. The distance between two adjacent sand-wave ridges is considered the sand-wave wavelength, the direction perpendicular to the sand-wave ridge is the sand-wave direction, and the ridge length is measured along the sand-wave ridge. The direction and ridge length of each sand wave are calculated by spatial topology analysis on the ArcGIS platform.

2.4 *Statistical Analysis of Sand Waves*

Based on the sand waves and their parameters, their spatial distribution is statistically analyzed. The schematic process of statistical analysis of sand waves is shown in Fig. 4, which involves a simple assumption that the original direction is the north and the direction angle increases clockwise, so the eastern direction is referred to as 90 deg. First, the study area is divided into 10 km × 10 km cells. A cell of HJ-1B sun glitter image and the corresponding sand waves are shown in Figs. 4(a) and 4(b), respectively. Then, the average wave direction of each cell is calculated by averaging all the sand-wave directions in the cell. The average direction is regarded as a representative direction of all the sand waves in the cell, as shown in Fig. 4(c). Third, a typical profile with the cell representative direction is selected, covering all the sand waves in the

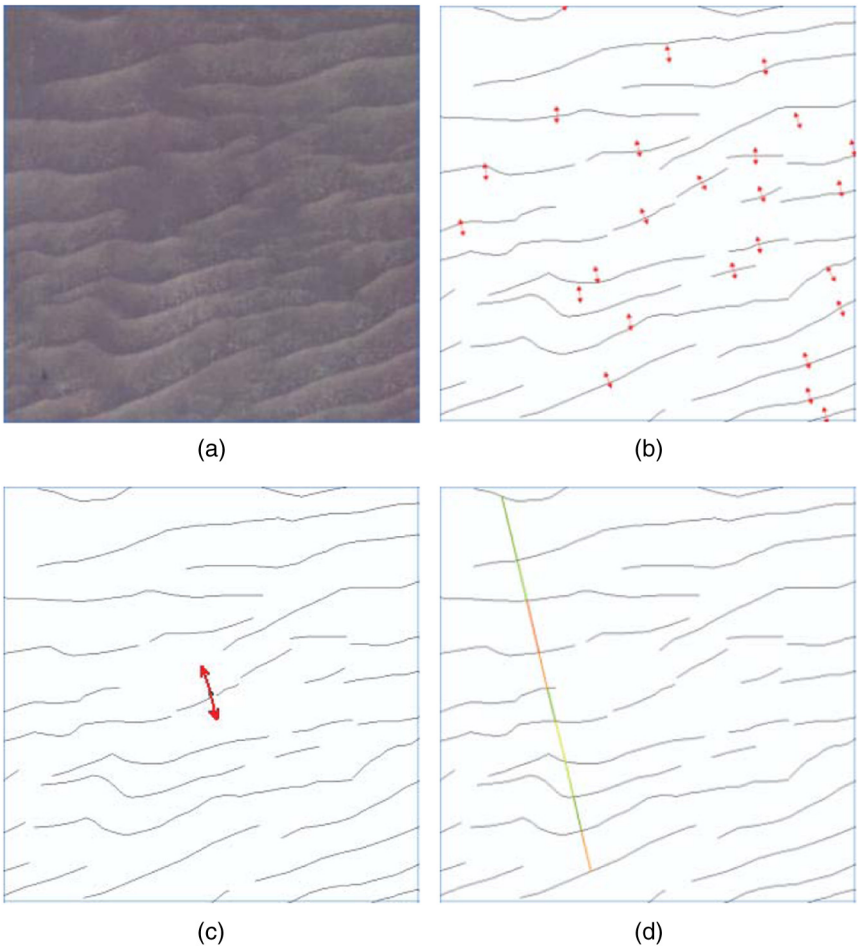

Fig. 4 Schematic diagram of statistical analysis of sand waves. (a) A cell of 10 km by 10 km of HJ-1B sun glitter image. (b) The sand waves determined from the image of (a). (c) The representative sand-wave direction of the cell. (d) A typical profile along the direction of (c), and the representative wavelength calculated by averaging the individual wavelength along the profile.

cell [Fig. 4(d)]. The average wavelength of the cell is obtained by averaging the sand-wave lengths along a typical profile. The average density (km^{-2}) is calculated from the ratio of the sand-wave number to area (100 km^2).

3 Results Obtained from Determining the Sand Waves

3.1 *Spatial Distribution of Sand Waves*

The sand waves in the TB are determined and mapped using the six HJ-1A/1B images listed in Table 1, leading to the identification of a total of 4604 sand waves, which are within 117°14' and 119°26'E, and 22°32.5' and 23°49'N, with an east-west span of up to 228 km and a north-south span of 145 km (Fig. 5). An envelope of all the sand-wave ridges is rendered in order to obtain the distribution range of the sand waves in the TB and its area. The area of the TB has, thus, been estimated to be 16,400 km^2, which is significantly larger than the previously reported value (~13,000 km^2).[14] Further details of the sand waves in the TB are revealed by our analysis, especially in the northeastern, western, and northwestern parts, where little investigation has previously been carried out. With the advantage of a large swath and high temporal repeatability of HJ-1A/1B, the sand waves can be mapped more comprehensively and the highest degree of accuracy thus far is achievable for the calculation of the sand-wave spatial cover.

3.2 *Spatial Characteristics of Sand Waves*

The spatial distribution of the sand-wave direction in the TB is illustrated in Fig. 6(a), and its histogram and probability rose diagram are shown in Figs. 6(b) and 6(c), respectively. The results from statistical analysis show that the sand-wave directions follow a normal distribution and range from 132 to 264 deg clockwise from the north (same as below), with an average direction of 190 deg and a standard deviation (STD) of 20.4 deg. In terms of the spatial distribution, the directions in the northwestern area of the TB are mostly >190 deg and those in the southeastern area are predominantly <190 deg.

A total of 1449 sand-wave wavelengths in the TB are obtained by applying the method described in Sec. 2.4. The spatial map and histogram of the wavelengths are shown in Fig. 7. The results from statistical analysis reveal a skewed distribution of the sand-wave wavelengths, which range from 76 to 2151 m, with a peak at 500 m and an average of 721 m. Regarding the spatial distribution, the wavelengths in the northwestern area of the TB are mostly >700 m, while those in the southeastern area are mostly <700 m.

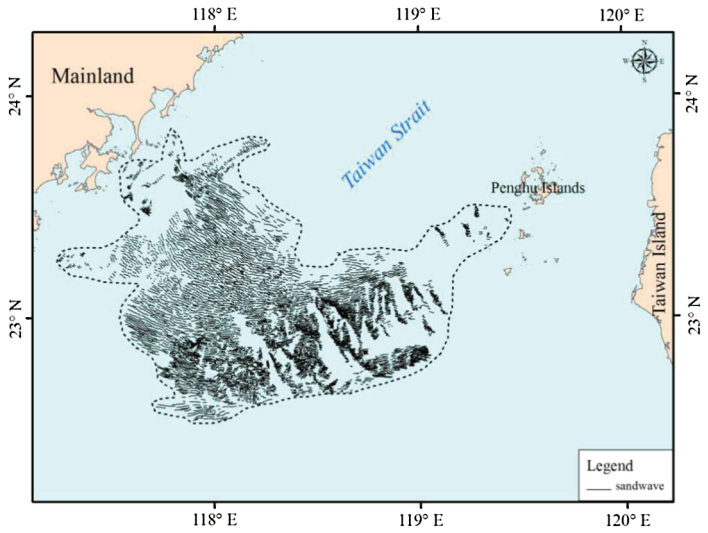

Fig. 5 Spatial distribution of the sand waves in TB. An envelope by the dashed line indicates the boundary of TB.

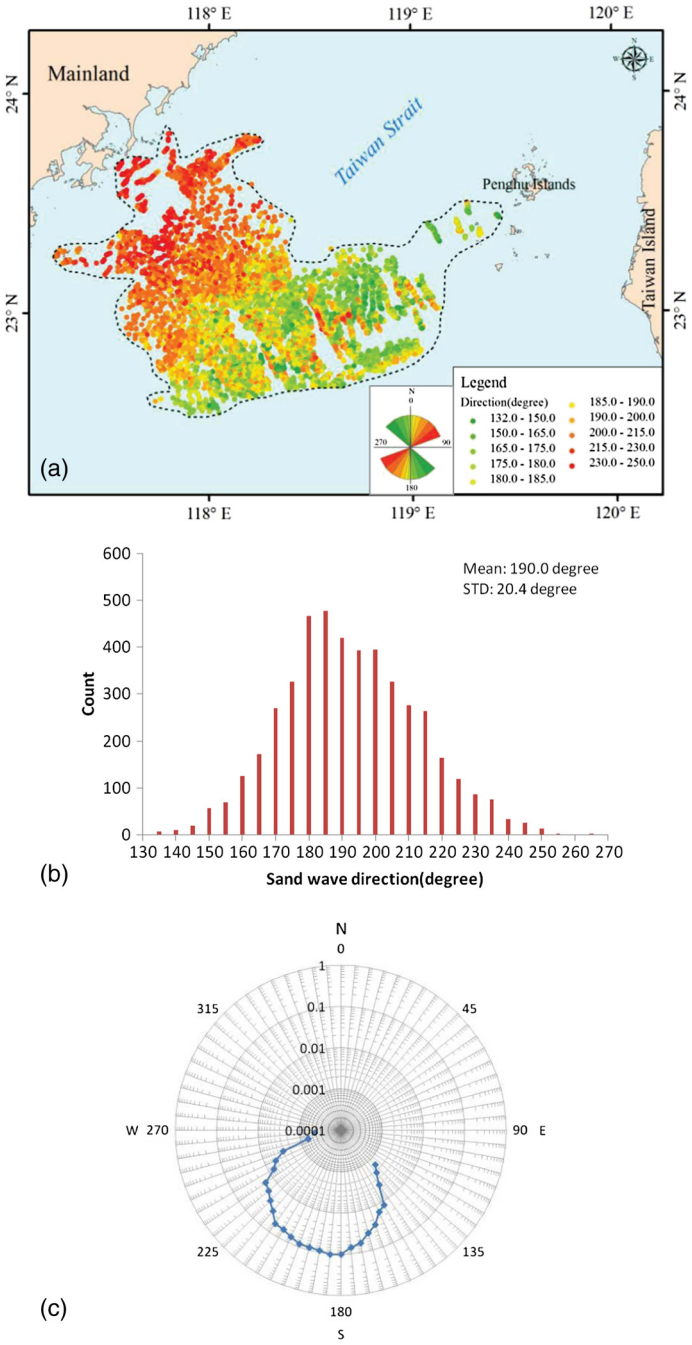

Fig. 6 Spatial distribution (a), histogram (b), and probability rose diagram (c) of sand-wave directions in TB.

Following the method described in Sec. 2.4, the average densities of 10-km grids are calculated, the distribution and density of which are shown in Fig. 8. Statistical analysis shows that the density also has a skewed distribution. The average density ranges from 0.035 to 1.090 km^{-2}, with an average of 0.359 km^{-2} and an STD of 0.221 km^{-2}, which implies that in the TB there are at least three or four sand waves in a 10-km grid (of 100 km^{-2}), and at the most 109 sand waves. Regarding the spatial distribution, the density of the southeastern area of the TB is relatively higher. Moreover, the density along the boundary of the TB is lower, generally <0.200 km^{-2}.

The ridge length of each sand wave is calculated by spatial topological analysis. All the sand-wave ridges in the TB are illustrated in Fig. 9(a), and the histogram of the ridge length

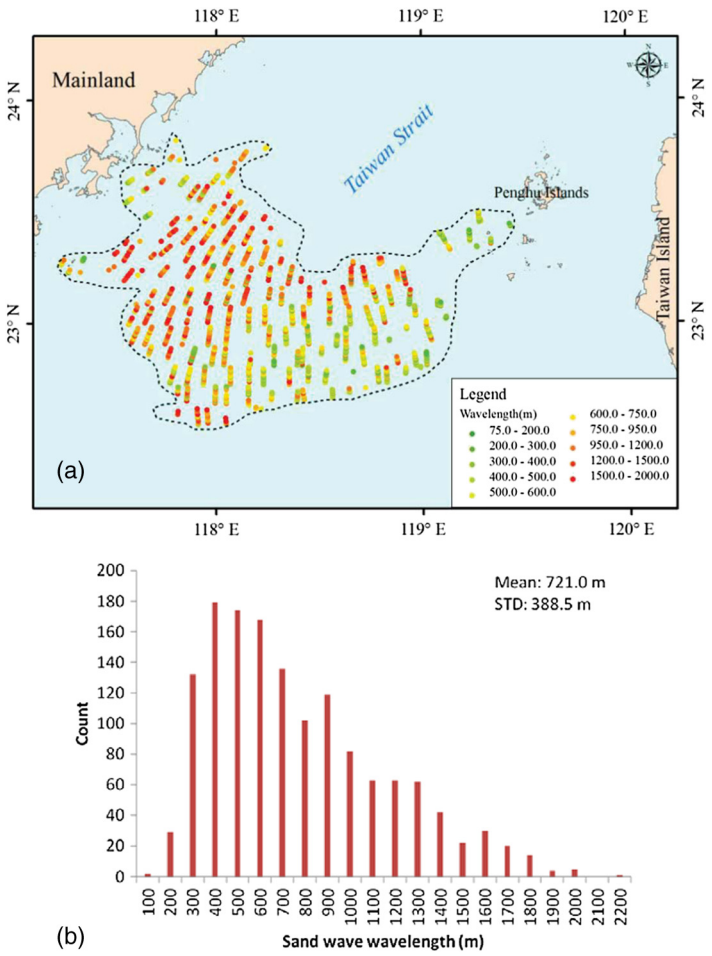

Fig. 7 Spatial distribution map (a) and histogram (b) of sand-wave wavelengths in TB.

distribution is shown in Fig. 9(b). Statistical analysis shows that ridge length has a strongly skewed distribution, being mostly <3000 m. The ridge length ranges from 254 to 19,992 m, with the peak distribution at ~1500 m and the average at 2453 m. Spatially, the sand waves with a ridge length <3000 m are distributed in the whole area of the TB, and those with a ridge length >10 km are observed in three regions, namely, the northwestern, the southwestern, and the northeastern regions.

4 Current Regime

The current is an important factor in determining the morphology and heterogeneous distribution of a sediment body.[23] The Taiwan Strait is located between mainland China and the Taiwan Island, and links the East China Sea in the north to the South China Sea in the south. The current regime in the Taiwan Strait is dominated by a semidiurnal tide and the M_2 tide which is the strongest and attracts a significant amount of research. Liand and Wang suggested that the M_2 tide in the Taiwan Strait is stronger than 1.0 m/s and is predominantly caused by the Kelvin waves from the East China Sea and the South China Sea.[26]

In order to understand the current regime in the TB, a hydrodynamic model is constructed on the basis of the semi-implicit Eulerian-Lagrangian finite-element model.[27] The hydrodynamic model covers the whole Taiwan Strait and the northeastern part of the South China Sea, with the TB as the core region of the model. The model contains 35,465 irregular grid nodes, and the grid cell size in the TB is ~1 km. Following results from previous research, the M_2 tidal current data are presented and analyzed here.

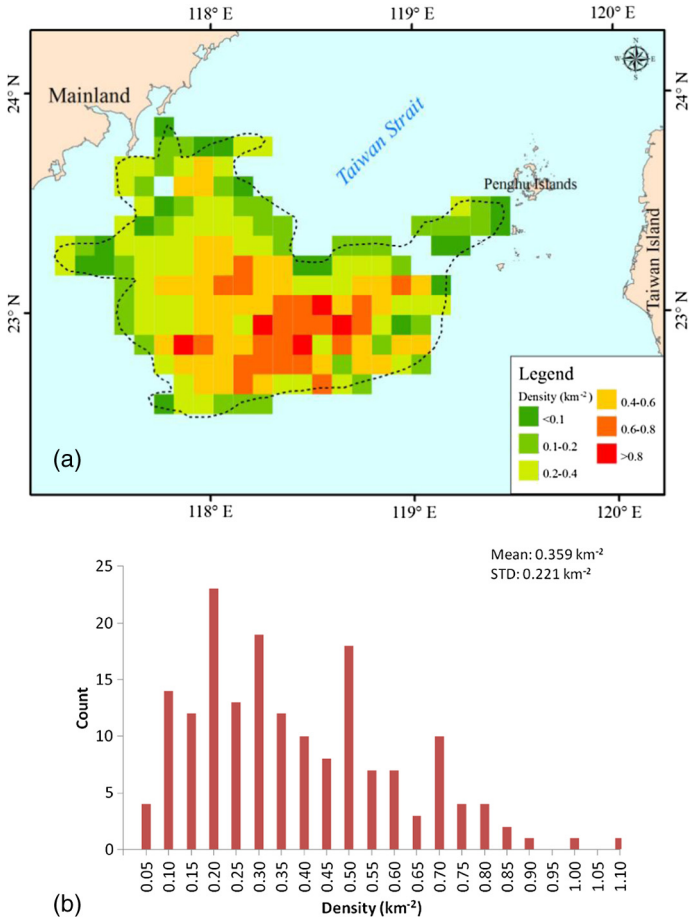

Fig. 8 Spatial distribution (a) and histogram (b) of sand-wave density in TB.

The M_2 tidal current ellipses of the bottom current and the vertical mean current are used for further analysis (Fig. 10). The bottom current data show that the average absolute current strength of the principal axis and the shortest axis are 0.51 and 0.12 m/s, respectively, and that the STDs are 0.12 and 0.08 m/s, respectively. The vertical mean current data show that the average absolute current strength of the principal axis and the shortest axis are 0.92 and 0.24 m/s, respectively, and that the STDs are 0.27 and 0.13 m/s, respectively. The ellipse ratio, i.e., the principal axis ratio (PAR), which is defined as the ratio of the shortest axis to the longest axis of the current speed, varies between zero and one. When the value of PAR approaches zero, the current represents a strong principal axis, whereas values approaching 1.0 indicate a circular current and frequent variations in the current direction. Both the bottom current and the vertical mean current show that the principal axis current (PAC) is significant in the TB (Fig. 10). The principal axis varies from north-south direction in the southeastern subregion to northeast-southwest direction in the northwestern subregion. The PAR values also differ between the two subregions, with smaller values in the northwestern subregion and larger values in the southeastern subregion. Therefore, the principal axis of the current in the northwestern subregion is stronger.

5 Analysis and Discussion

5.1 *Regional Division of the Taiwan Banks*

As shown in Figs. 6 to 9, the direction, wavelength, density, and ridge length of the sand waves differ from one region to another. Figure 11 illustrates the distribution of direction and wavelength of the sand waves in the 10-km grid. The sand waves in the northwestern subregion of the

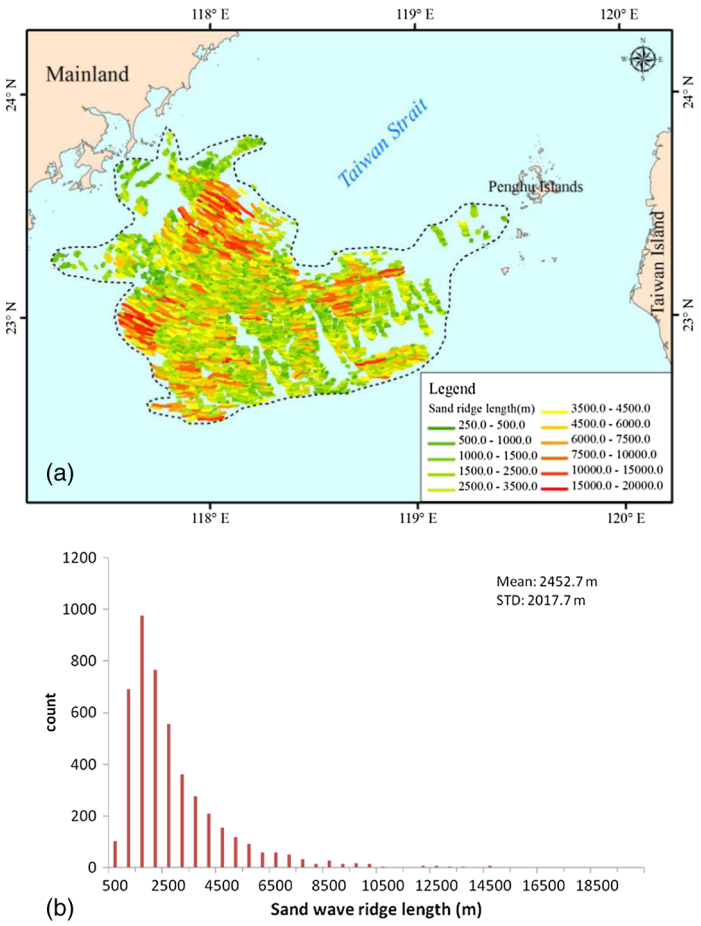

Fig. 9 Spatial distribution (a) and histogram (b) of sand-wave ridge length in TB.

TB display a northeast-southwest direction, while those in the southeastern subregion are oriented in a north-south direction.

Two different subregions in the TB in terms of direction and wavelength of the sand waves is, therefore, obvious (Fig. 11). The northwestern and southeastern subregions have areas of ~7400 km^2 and 9000 km^2, respectively. There are 1495 sand waves in the northwestern subregion, which is about one third of the total number of sand waves in the TB. There are 3109 sand waves in the southeastern subregion.

5.2 *Statistical Analysis of Sand Waves*

Following the division of the TB into two subregions, some statistical analyses of sand-wave direction, wavelength, density, and ridge length in the two subregions were performed and the results are listed in Table 2.

The count histogram of directions and the probability rose diagram in the subregions are illustrated in Fig. 12. The sand waves in both subregions follow a normal distribution. In the northwestern subregion, the sand waves are mainly aligned in the northeast-southwest direction, with an average direction of 210 deg, while >50% of the directions range from 200 to 220 deg. The average direction in the southeastern subregion is 180 deg and >50% of the directions range from 170 to 190 deg.

The wavelengths in the two subregions have distinct distributions, as illustrated by the histograms (Fig. 13). The wavelengths in the northwestern subregion are between 600 and 1250 m, while those in the southeastern subregion are relatively shorter, between 350 and 900 m. The average wavelength in the northwestern subregion is 950 m, much longer than that in the southeastern subregion (610 m). The histogram also reveals that the wavelength of 900 m is

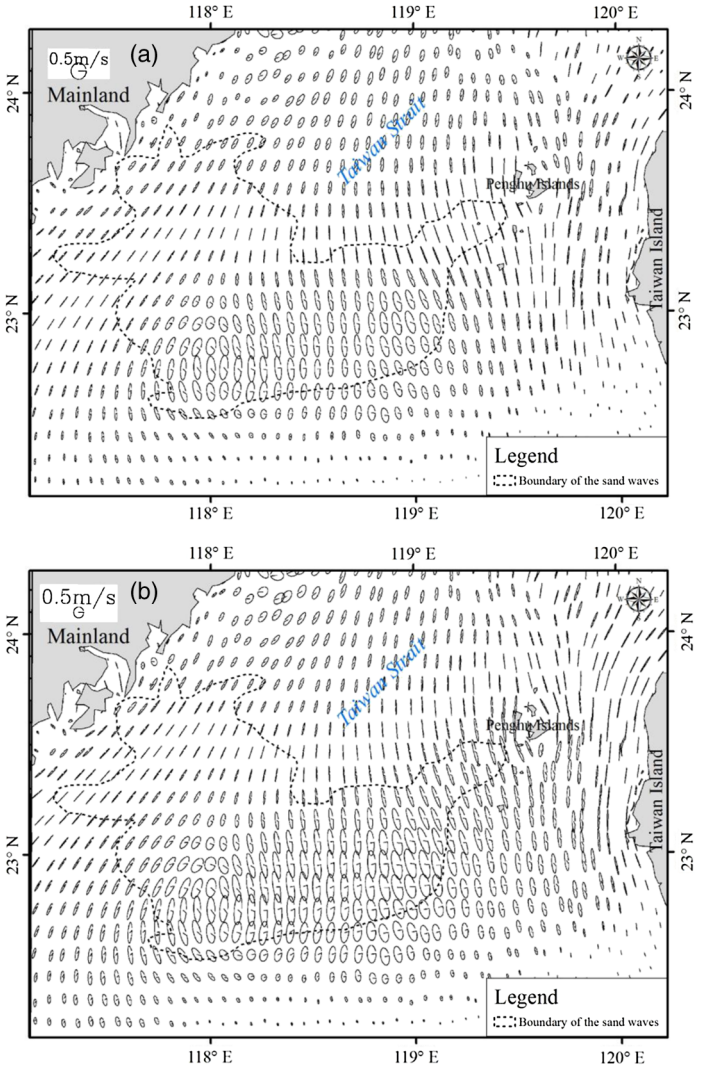

Fig. 10 Pattern of the M_2 tidal current ellipses in the Taiwan Strait from the hydrodynamic model: (a) bottom current and (b) vertical mean current. The direction of the principal axis of current ellipse is the dominant current direction, and the length of the longest axis of current ellipse is the current velocity.

a dividing crest. The wavelengths <900 m in the southeastern subregion are significantly more abundant than in the northwestern subregion, while those >900 m are more abundant in the northwestern subregion than in the southeastern subregion.

The count histograms of density in the two subregions illustrate that the average density in the southeastern subregion ranges from 0 to 1.1, with an average of 0.438, while that in the northwestern subregion ranges from 0.1 to 0.7, with an average of 0.294 [Fig. 14(a)]. Overall, the density in the southeastern subregion is comparatively higher. Both density and wavelength can describe the sand-wave development. A scatter diagram of wavelength versus density is plotted in Fig. 14(b). In the low-density areas, the wavelengths vary widely from 200 to 2000 m. However, in the areas of higher density, the sand waves consistently have shorter wavelengths. Therefore, although there are fewer sand waves in the low-density area, their wavelengths may be long or short. In the high-density area, the sand waves are more abundant, and the wavelengths (distance between two adjacent sand-wave ridges) are shorter.

The average ridge lengths of the sand waves and their ranges in the two subregions are similar (Table 2, Fig. 15), but long ridges are more abundant in the northwestern subregion. The ridge-length frequency distribution for each subregion is determined by plotting the exceedance probability versus length. This parameter represents the probability (y axis) that a given sand wave

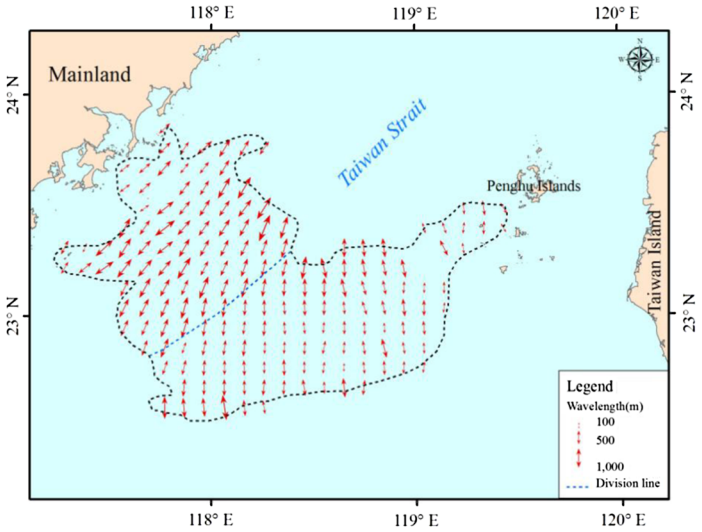

Fig. 11 Spatial distributions of direction and wavelength of the sand waves in 10-km grid. TB can be divided into two subregions in terms of direction and wavelength of the sand waves. The direction and length of each red double-head arrow represent the average direction and average wavelength of sand waves in a 10-km grid, respectively.

will be equal to or greater than a given length[23] [x axis; Fig. 15(b)]. For each subregion, the ridge-length frequency distribution shows a large number of short sand-wave ridges and a small number of longer structures. However, the northwestern subregion contains fewer long sand-wave ridges. For example, a given sand-wave ridge in the northwestern subregion has a 10% probability (exceedance probability > 0.90) of being equal to or longer than 6000 m. A ridge in the southeastern subregion, however, has an equivalent probability of being only 4500 m (or longer). In other words, the ridge lengths >5 km account for 12.5% in the northwestern subregion and only 7.8% in the southeastern subregion. The ridge lengths >10 km account for 2.1 and 0.4% in the northwestern subregion and southeastern subregion, respectively.

5.3 *Hydrodynamic Influence on Sand Waves*

The tidal nature of the bottom current is an important factor in the heterogeneous distribution of sand-wave features in the TB. The large-scale sand waves represent certain obstacles for the bottom current. Interactions between currents and sand waves may affect sand-wave features, such as direction, wavelength, density, and ridge length. The direction of current, PAC speed,

Table 2 Direction, wavelength, density, and ridge length of sand waves in the two subregions of the Taiwan Banks.

Subregion	Parameters	Minimum	Maximum	Mean	Main ranges
Northwestern	Direction (deg)	139	264	210	200 to 220
	Wavelength (m)	80	2151	950	400 to 1400
	Density (km^{-2})	0.056	0.700	0.294	0.200 to 0.500
	Ridge length (m)	254	19,992	2773	700 to 2250
Southeastern	Direction (deg)	133	239	180	170 to 190
	Wavelength (m)	76	1914	610	350 to 900
	Density (km^{-2})	0.035	1.090	0.438	0.200 to 0.700
	Ridge length (m)	274	15,017	2338	600 to 2300

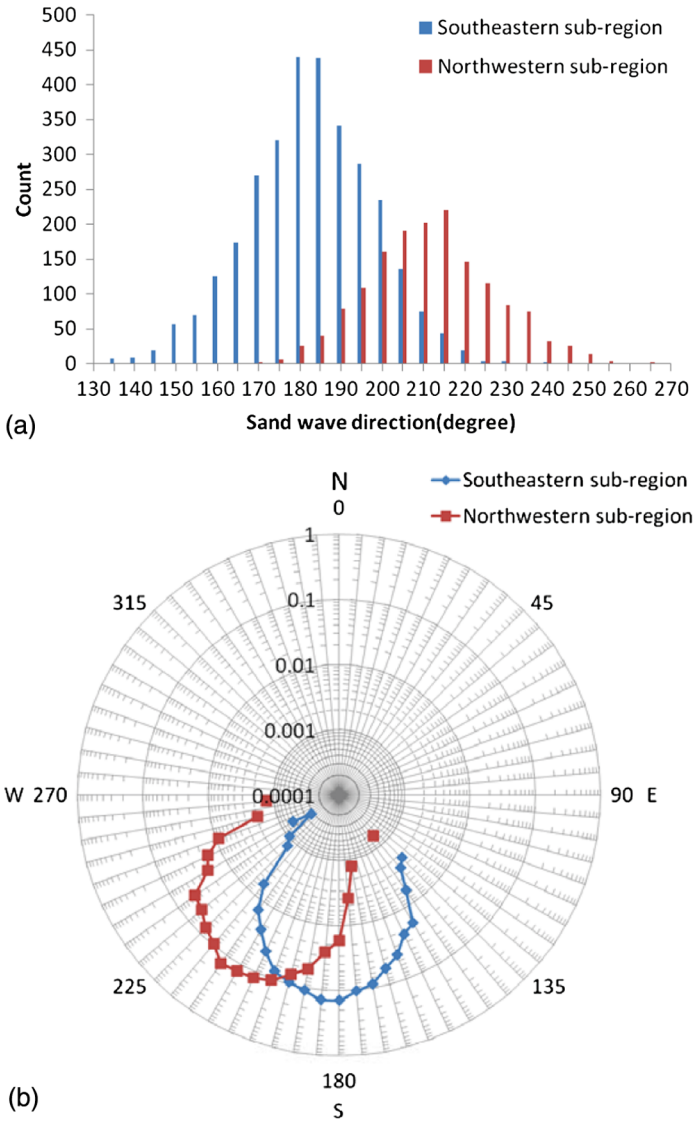

Fig. 12 Count histogram (a) and probability rose diagram (b) of sand-wave directions in the two subregions.

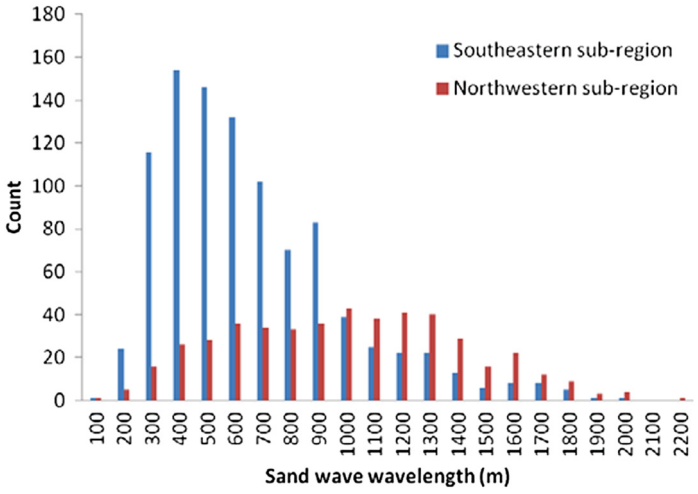

Fig. 13 Count histogram of sand-wave wavelength in the two subregions.

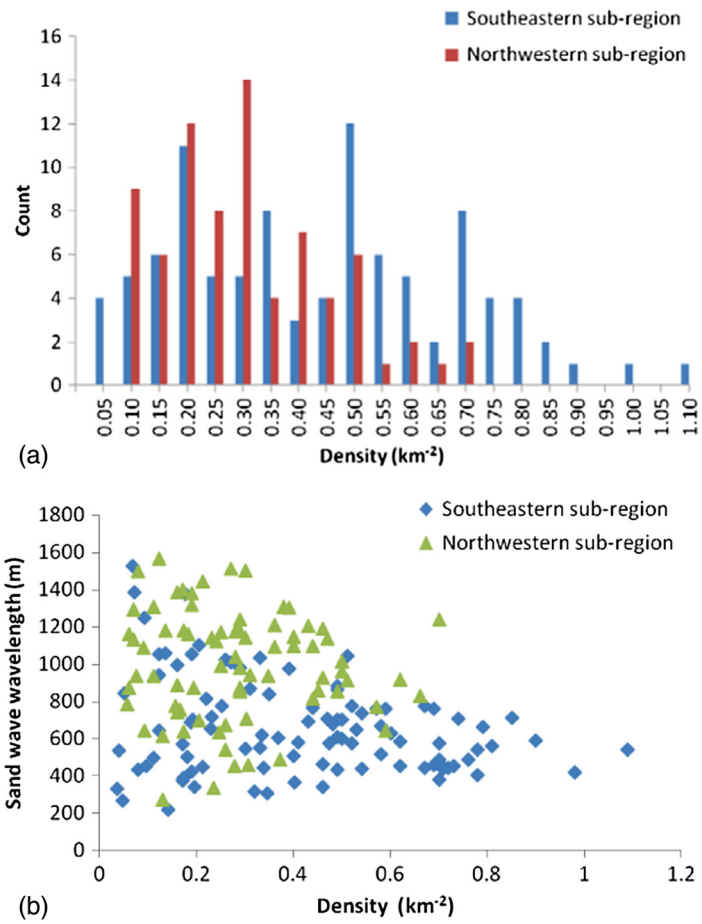

Fig. 14 Count histogram of sand-wave density in the two subregions (a) and wavelength versus density of the sand waves in the two subregions.

and PAR of the current are three important parameters of the current regime. Here, quantitative analyses of bottom-current data against various sand-wave parameters are presented.

The average direction of PAC and the average direction of sand waves are derived from each 10-km grid, and they have a considerable correlation ($R^2 = 0.7643$; Fig. 16). In the northwestern subregion, the two directions are in the northeast-southwest direction, while in the southeastern subregion, they are along the north-south direction. According to previous studies,[28–30] the current in the northwestern subregion is dominated by a coastal current along the mainland coast in the northeast-southwest direction, while the current in the southeastern subregion flows closely along the north-south direction in most seasons. Results obtained by Shao confirmed that the sand-wave directions are generally aligned along the current directions in the TB.[7] Therefore, the current is the dominant force for sand-wave formation in the TB, and its dominant direction controls the sand-wave orientation.

The PAC strength is another important factor for sand-wave shape and distribution. The quantitative relationships between PAC speed and wavelength, density, and ridge length are shown in Fig. 17, which do not show any significant correlations. All three correlation coefficients are low ($R^2 = 0.2673/R^2 = 0.1933/R^2 = 0.0310$). Wavelength has a very weak negative correlation with the PAC speed, whereas density has a very weak positive correlation. A larger current speed could induce a stronger disturbance on the bottom sediment, and the sediment particles may be frequently resuspended and deposited. The physical process has an impact on the formation of sand waves, resulting in smaller spacing and higher density.

Another parameter of current regime is the PAR of the current, which is used to describe the frequency of varying current directions. The quantitative relationships between PAR and wavelength, density, and ridge length are shown in Fig. 18, where no significant correlations are

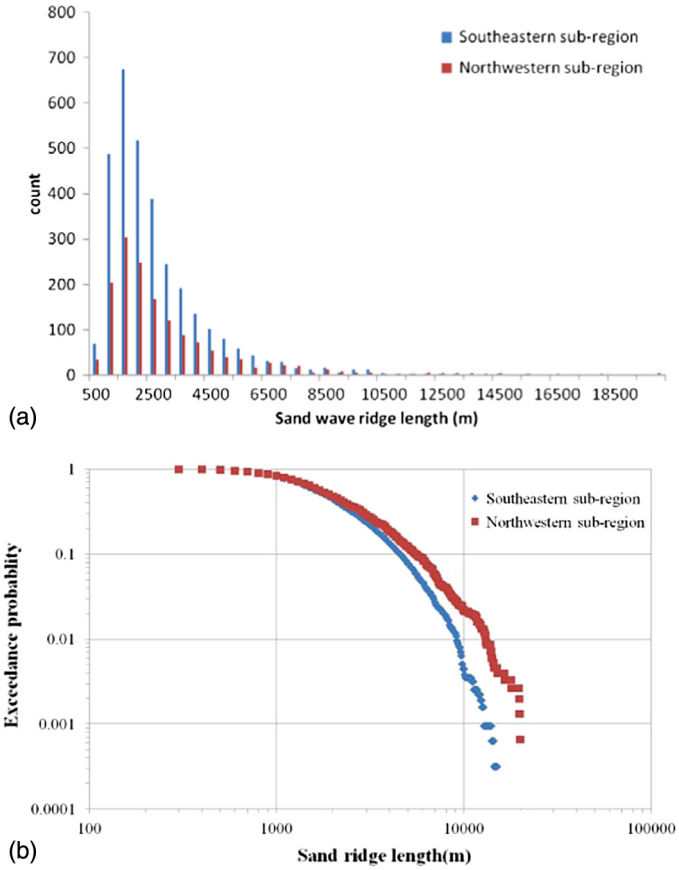

Fig. 15 Count histogram of sand-wave ridge length in the two subregions (a) and log-log plot of ridge length versus exceedance probability (b). In (b), the *y* axis represents the probability that a given ridge is equal to or longer than a given area (*x* axis). Exceedance probability is calculated based on the observed length frequency distribution of sand waves in each subregion.

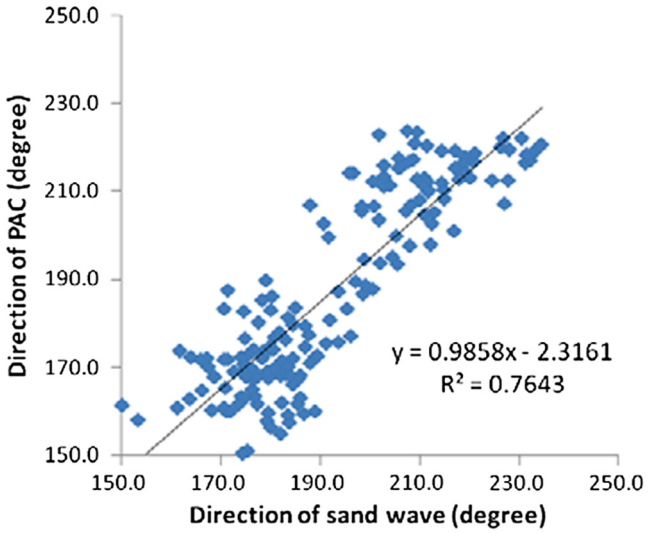

Fig. 16 Plot of direction of sand wave versus direction of principal axis current (PAC). There is a strong positive correlation ($R^2 = 0.7643$) between the two directions.

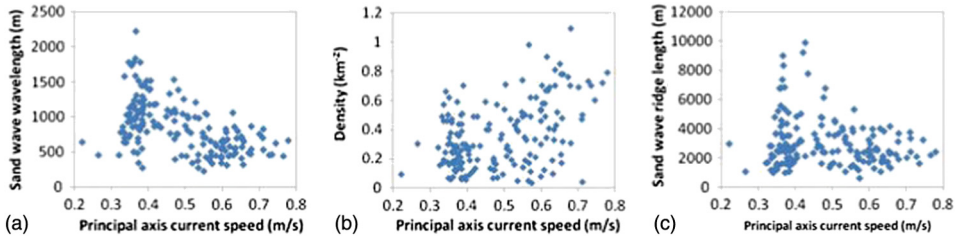

Fig. 17 Plots of PAC speed versus wavelength (a), density (b), or ridge length (c). All three correlation coefficients are very low.

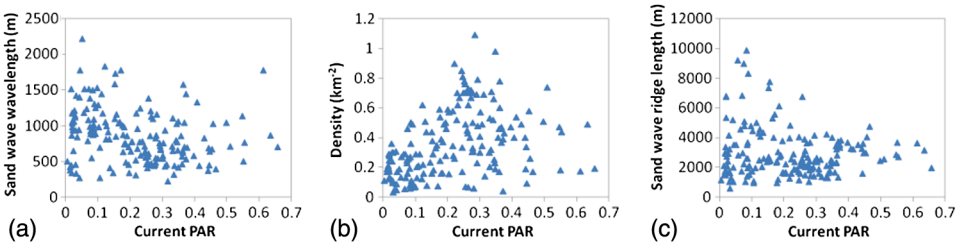

Fig. 18 Plots of current principal axis ratio versus wavelength (a), density (b), or ridge length (c). All three correlation coefficients are very low.

observed. The highest correlation coefficient is only 0.1340 (R^2) between PAR and density. The plot depicts a weak trend, namely, a slowly increasing density with increasing PAR. It is also evident that both longer wavelengths and ridge lengths are distributed in the lower PAR area. For example, almost all the wavelengths >1300 m and ridge lengths >4000 m are located in the area with PAR <0.3. In these smaller PAR areas, the PAC is strong and the current direction is more stable. The more stable direction is an advantage for the formation of larger sand waves (longer wavelength and ridge length), and therefore, it is one of the essential conditions. In contrast, the higher PAR could induce a stronger disturbance on the bottom sediment, and the sediment particles may frequently get resuspended and deposited under the current with varying directions. The result shows that shorter wavelength and ridge length as well as higher density exist in higher PAR areas.

The above correlation analysis indicates that the direction of the sand waves is consistent with the direction of the dominant current. Even when the dominant current and PAR do not significantly determine the shape, size, and distribution of the sand waves, hydrodynamic conditions still influence sand waves to a certain degree.

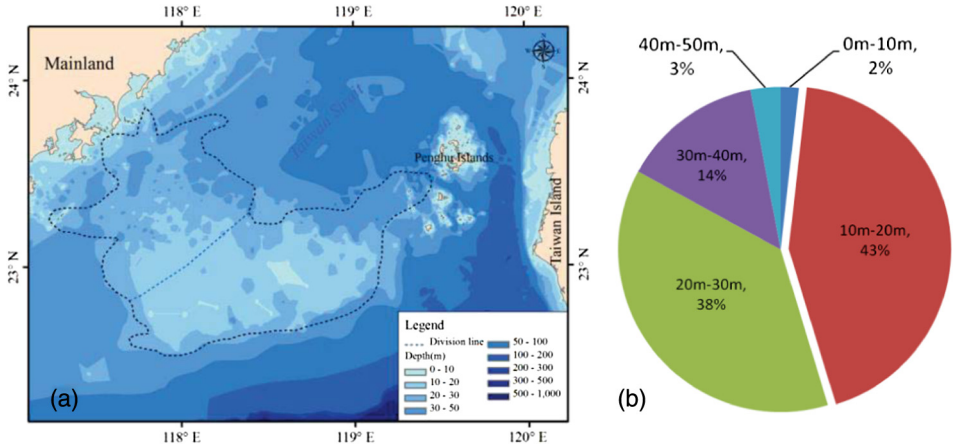

Fig. 19 Spatial distribution of water depth and boundary in TB (a) and probability of different depths in TB (b).

5.4 *Water Depth Influence on Sand Wave*

In addition to the controlling effect of the tidal current, water depth is another important influencing factor on sand waves. Previous research on the TB had revealed that longer-wavelength sand waves exist in the deeper water region, and shorter-wavelength sand waves exist in the shallow water region.[7] For example, the western TB has deeper water depths, with an average depth of 35 m, longer wavelength (1000 to 1800 m), and lower amplitude (<6 m), while the eastern TB has relatively a shallower water depth (<15 m), shorter wavelength (500 to 1000 m), and higher amplitude (average of 15 m). The current study, based on comprehensive sand-wave information, attempts to discuss the distribution of sand waves in different water depths and analyze the correlation between water depth and wavelength, density, and ridge length.

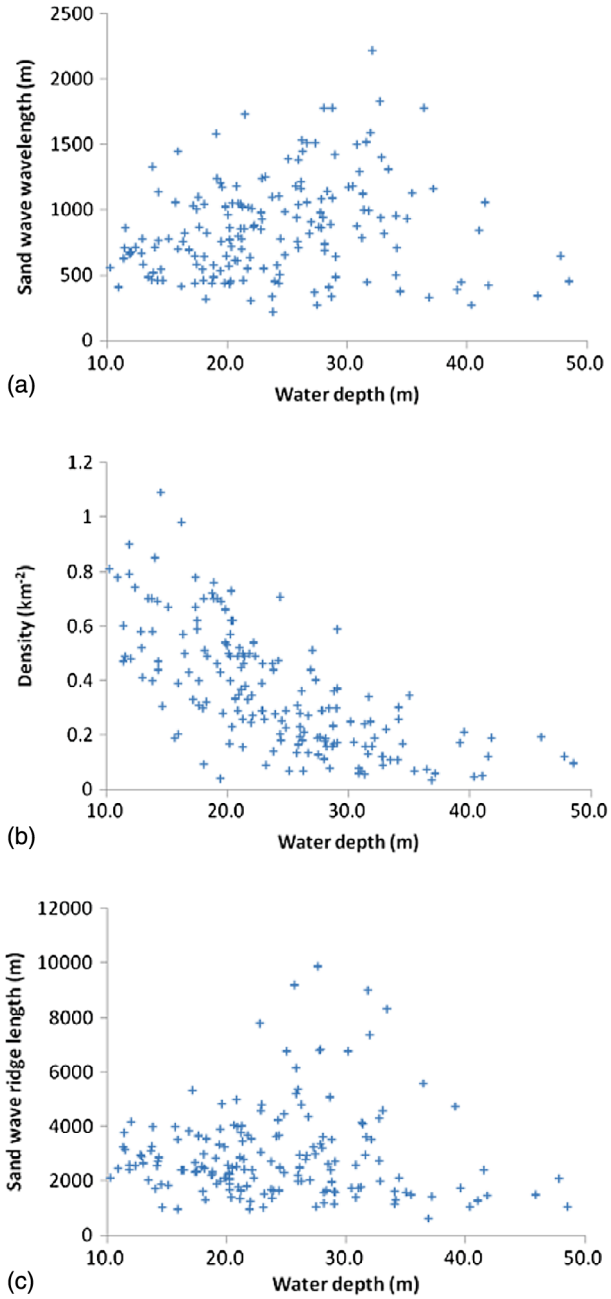

Fig. 20 Plots of water depth versus wavelength (a), density (b), or ridge length (c). Only the sand-wave density has certain negative correlation with water depth ($R^2 = 0.4677$).

By overlaying the boundary of the sand waves on the water-depth map obtained from nautical charts [Fig. 19(a)], it is revealed that the water depths of the sand-wave region primarily range from 10 to 50 m, with an average of 23.3 m. Most of the area with a depth from 10 to 30 m is covered by sand waves. The probability of a different water-depth area is calculated and shown in Fig. 19(b). Among them, the highest probability is 43% at a depth range from 20 to 30 m, which covers about half of the area in the TB. The next depth range is from 10 to 20 m, ~38%, and is mainly located in the western TB. The area deeper than 30 m is ~17% and is distributed along the boundary of the TB. There is only an ~2% area shallower than 10 m in the central TB.

The average water depths of 10-km grids are derived and used to analyze the correlation between water depth and wavelength, density, and ridge length. The results are plotted in Fig. 20. Among them, the density has a certain negative correlation with the water depth ($R^2 = 0.4677$), which indicates that the density in shallow water is higher than that in deep water. Though the other two correlation coefficients are very low, the scatter diagrams still reveal that numerous sand waves are developed in shallow water (10 to 20 m) and that the sand waves with long wavelengths or ridge lengths are located in water with a depth close to 30 m. Considering the above analysis, shallow water depth might be a necessary condition for intensive sand waves, but large-scale sand waves need a moderate depth, e.g., 30 m.

6 Conclusions

This study demonstrates the possibility of making full use of the satellite remote sensing technology with large swath width and rapid coverage by using HJ-1A/1B CCD sun glitter imagery to observe the sand waves in the TB as completely as possible, to obtain the direction, wavelength, density, and ridge length of sand waves, to analyze their spatial distributions, and to understand the roles of the current and the water depth in shaping sand waves. Six cloud-free HJ-1A/1B CCD sun glitter images were selected from >250 images and processed to study the sand waves in the TB. A total of 4604 sand waves were identified covering an area of ~16,400 km^2, larger than the previous result of the size of the TB based on an incomplete in-site survey. This is the first time that such a full coverage of the sand-wave information in the TB has been achieved, including the most comprehensive information on their direction, wavelength, density, and ridge length.

The direction, wavelength, density, and ridge length of the sand waves in the TB were mapped and analyzed. Due to the differences in the spatial distribution of the wavelength and direction of the sand waves, the TB was divided into two subregions; northwest and southeast. The sand-wave directions have a normal distribution in the whole TB, and the average direction is 190 deg. However, the average direction of the sand waves in the northwestern subregion was along the northeast-southwest direction, while that in the southeastern subregion was along the north-south direction. The average wavelength in the TB is 721 m, but that in the northwestern subregion is 950 m, longer than the average wavelength in the southeastern subregion of 610 m. The density in the southeastern subregion is higher than that in the northwestern subregion. The average ridge lengths and ranges of the sand waves in the two subregions are similar, but the northwestern subregion has longer ridge length sand waves.

The relationships between the spatial distribution of the sand waves and both the tidal current data from numerical simulation and water depth from nautical charts were also analyzed, and some interesting conclusions were obtained. The directions of sand waves are consistent with the directions of the PAC, which indicates that the orientation of sand waves is controlled by the current. The other correlations are not significant enough to draw solid conclusions, but hydrodynamic conditions and water depth can influence the sand waves to a certain degree. The higher density of sand waves tends to appear under a stronger current, higher PAR of the current, and shallower water (10 to 20 m). Another conclusion is that the sand waves with longer wavelengths or ridge lengths are always located in the area with the lower PAC, more stable direction of current, and moderate depth (e.g., 30 m). While these findings are interesting, these datasets show that the factors and processes responsible for the variability in sand waves are complex and need further study.

Acknowledgments

This research was supported by a grant from the Public Science and Technology Research Fund Project of Ocean (201105001), the National Nature Science Foundation of China (Grant 91128204), and the Public Technology Research Fund Project of Zhejiang Province (2014C31016). The HJ-1A/1B data used in this article were provided from the China Centre for Resources Satellite Data and Application. The authors would like to thank Dr. Zuojun Yu for improving the presentation of the paper. They would also like to thank two anonymous reviewers who provided substantial comments to help improve the manuscript.

References

1. B. R. Calder et al., "Automatic processing of high-rate, high-density multibeam echosounder data," *Geochem., Geophys., Geosyst.* **4**(6), 24–48 (2003).
2. S. Passchier et al., "Observations of sand waves, megaripples, and hummocks in the Dutch coastal area and their relation to currents and combined flow conditions," *J. Geophys. Res.* **110**(F4), F04S15 (2005).
3. J. P. Xu et al., "Sandwave migration in Monterey submarine canyon, central California," *Mar. Geol.* **248**(3–4), 193–212 (2008).
4. W. Yu, "Study on meticulous shape characteristics and migration of sand waves in the Taiwan Banks," MS Thesis, The Second Institute of Oceanography, SOA, China (2013).
5. Z. C. Liu et al., "The development in the latest technique of shallow water multi-beam sounding system," *Hydrogr. Surv. Charting* **25**, 67–70 (2005) (Chinese).
6. I. Hennings et al., "Sun glitter radiance and radar cross-section modulations of the sea bed," *J. Geophys. Res.* **99**(C8), 16303–16326 (1994).
7. H. Shao, "Study of sand waves in the Taiwan Banks through observation of sun glitter," Ph.D. Thesis, Xiamen University, Xiamen, China (2011).
8. Z. H. Mao, D. F. Guo, and D. L. Pan, "A study of sun glitter obtaining and removing in airborne ocean color remote sensing," *Remote Sens. Technol. Appl.* **11**(4), 15–20 (1996) (Chinese).
9. C. R. Jackson et al., "The role of the critical angle in brightness reversals on sunglint images of the sea surface," *J. Geophys. Res.* **115**(C9), C09019 (2010).
10. M. Christian et al., "Sun glitter in SPOT images and the visibility of oceanic phenomena," in *Proc. 22nd Asian Conf. on Remote Sensing*, Singapore, pp. 870–875 (2001).
11. H. Shao et al., "Sun glitter imaging of submarine sand waves on the Taiwan Banks: determination of the relaxation rate of short waves," *J. Geophys. Res.* **116**(C6), C06024 (2011).
12. S. Boggs, "Sand-wave fields in Taiwan Strait," *Geology* **2**, 251–253 (1974).
13. Z. X. Liu, "The progress of China shelf tidal deposits," *Adv. Earth Sci.* **11**(4), 414–416 (1996) (Chinese).
14. Y. L. Lin et al., "The Taiwan Straits wave facts," *J. Oceanogr. Taiwan Strait* **2**(1), 20–28 (1983) (Chinese).
15. X. Q. Du et al., "Characteristics of the large-scale sandwaves, tidal flow structure and bedload transport over the Taiwan Banks in southern China," *Acta Oceanol. Sin.* **30**(5), 124–137 (2008).
16. F. L. Li, "Annual variations of Secchi depth in the nearshore waters of the western Taiwan Strait during the summers of 1998 ~ 2010," *J. Oceanogr. Taiwan Strait* **31**(3), 301–306 (2012) (Chinese).
17. Y. Li et al., "Study on stability of sand waves by satellite sensing," in *Proc. of the First Asian and Pacific Coastal Engineering Conf.*, Dalian, China, Vol. 2, pp. 850–856 (2001).
18. B. Fu, "Shallow sea bottom topography mapping by SAR," Ph.D. Thesis, Ocean University of China, Qingdao, China (2005).
19. K. G. Fan, "Shallow water bathymetry surveys by SAR based on M4S for microwave scattering imaging oceanic surface," PhD Thesis, Ocean University of China, Qingdao, China (2009).
20. J. Yang et al., "A detection model of underwater topography with a series of SAR images acquired at different time," *Acta Oceanol. Sin.* **29**(4), 28–37 (2010).

21. J. Yang et al., "Underwater topography detection of Taiwan Shoal with SAR images," *Chin. J. Oceanol. Limnol.* **28**(3), 636–642 (2010).
22. Y. K. Lian, "On the activity of sand waves in the Taiwan Banks," MS Thesis, Xiamen University, Xiamen, China (2010).
23. T. B. S. Correa et al., "Variability of cold-water coral mounds in a high sediment input and tidal current regime, Straits of Florida," *Sedimentology* **59**(4), 1278–1304 (2012).
24. China Center for Resources Satellite Data and Application, "Introduction of HJ-1A/B," http://www.cresda.com/n16/n1130/n1582/8384.html (8 May 2009).
25. W. Alpers and I. Hennings, "A theory of the imaging mechanism of underwater bottom topography by real and synthetic aperture radar," *J. Geophys. Res.: Oceans* **89**(C6), 10529–10546 (1984).
26. L. Li and S. J. Wang, "Notes on the tidal current in the Taiwan Strait," *Oceanol. Et Limnol. Sin.* **21**(6), 578–580 (1990).
27. Y. Zhang and A. M. Baptista, "Selfe: a semi-implicit Eulerian–Lagrangian finite-element model for cross-scale ocean circulation," *Ocean Model.* **21**(3–4), 71–96 (2008).
28. S. Jan et al., "Seasonal variation of the circulation in the Taiwan Strait," *J. Mar. Syst.* **35**(3–4), 249–268 (2002).
29. L. Li et al., "Oceanic fronts in southern Taiwan Strait," *J. Oceanogr. Taiwan Strait* **19**(2), 147–156 (2000).
30. X. Q. Du et al., "Hydrodynamic processes and bed-load transport associated with large-scale sand waves in the Taiwan Strait," *J. Coastal Res.* **26**(4), 688–698 (2010).

Hua-guo Zhang is an associate professor of the Second Institute of Oceanography, State Oceanic Administration, China. His research interests include coastal remote sensing and GIS. He has published about 20 papers. He earned his BS in environment from Nankai University in 1999, his MS in oceanography at the Second Institute of Oceanography, State Oceanic Administration in 2002, and his PhD in oceanography from Ocean University of China in 2011.

Xiu-lin Lou is an associate professor of the Second Institute of Oceanography, State Oceanic Administration, China. His research interests include remote sensing of red tides, upwelling, and coastal environments. He received his PhD in remote sensing and satellite oceanography from the Ocean University of China in 2011.

Biographies of the other authors are not available.